ACS APPLIED MATERIALS & INTERFACES

Research Article

www.acsami.org

Structural Investigation of Cr(Al)N/SiO$_x$ Films Prepared on Si Substrates by Differential Pumping Cosputtering

Masahiro Kawasaki,*,† Hiroshi Takabatake,‡ Ichiro Onishi,§ Masateru Nose,⊥ and Makoto Shiojiri∥,○

†JEOL USA Inc., 11 Dearborn Road, Peabody, Massachusetts 01960, United States

‡School of Science and Engineering, University of Toyama, Toyama 930-8555, Japan

§JEOL Ltd., 3-1-2 Musashino, Akishima, Tokyo 196-8558, Japan

⊥Faculty of Art and Design, University of Toyama, Takaoka 933-8588, Japan

∥Kyoto Institute of Technology, Kyoto 606-8585, Japan

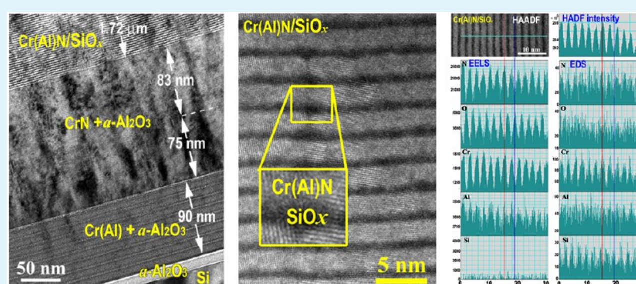

ABSTRACT: Analytical electron microscopy revealed the structure and growth of hard coating Cr(Al)N/SiO$_x$ nanocomposite films prepared in a differential pumping cosputtering (DPCS) system, which has two chambers to sputter different materials and a rotating substrate holder. The substrate holder was heated at 250 °C and rotated at a speed as low as 1 rpm. In order to promote the adhesion between the substrate and composite film, transition layers were deposited on a (001) Si substrate by sputtering from the CrAl target with an Ar flow and a mixture flow of Ar and N_2 (Ar/N_2) gases, subsequently, prior to the composite film deposition. Then, the Cr(Al)N/SiO$_x$ nanocomposite film was fabricated on the transition layers by cosputtering from the CrAl target with the Ar/N_2 gas flow and from the SiO_2 target with the Ar gas flow. The film had a multilayer structure of ~1.6 nm thick crystallite layers of Cr(Al)N similar to NaCl-type CrN and ~1 nm thick amorphous silicon oxide layers. The structure of the transition layers was also elucidated. These results can help with the fabrication of new hard nanocomposite films by DPCS.

KEYWORDS: *Cr(Al)N/SiO$_x$, cosputtering, nanocomposite film, hard coating, analytical electron microscopy*

1. INTRODUCTION

Nanocomposite films have been widely applied for optical,[1−3] electric,[4] magnetic,[5] optoelectronic[6,7] and photocatalytic devices[8] and hard coatings.[9,10] These films have been fabricated by several different techniques such as plasma enhanced chemical vapor deposition,[1,2,9] radiofrequency (reactive) sputtering deposition,[3−5,8,10] metal−organic chemical vapor deposition,[6] atomic layer deposition.[7] Recently, one of the present authors (M.N.) and his collaborators developed a differential pumping cosputtering (DPCS) system, which can fabricate nanocomposite or multilayered films with compositions not limited by thermodynamic restrictions.[11]

Nitrides of transition metals such as Ti, Zr, and Cr are known as materials for hard and superhard coatings.[12,13] Much attention has been devoted to studies of nanocomposite films of metal nitrides such as TiN/Si_3N_4, TiN/BN, and CrN/AlN due to their extreme hardness.[14,15] For example, Lin et al. who investigated the process, structure, and properties of nanostructured multifunctional tribological coatings used in different industrial applications, reported that superlattice CrN/AlN coating with a bilayer period of ~3 nm exhibits a super hardness of 45 GPa, showing the improve toughness and wear resistance of graded CrAlN coatings as compared to the homogeneous CrAlN coating.[15] In contrast, there are few reports on oxygen containing nanocomposite films, which are stable at higher temperatures, although CrAlON films have been studied.[16] It is difficult to obtain nanocomposite films consisting of nitride and oxide phases by conventional reactive sputtering methods because of the high reactivity of oxygen to aluminum or titanium.

In the previous paper, Nose et al. illustrated the details of the DPCS system with two chambers and evaluated theoretically and experimentally the Knudsen number of the clearance between the two chambers.[11] They showed that dividing gas atmospheres in this system greatly reduces cross-contamination, thus allowing for nitride and oxide to be codeposited by rapid rotation of the substrate. In this paper, we investigate the structure and growth of ultrathin films prepared by DPCS by means of analytical electron microscopy (EM). The sample was composed of a Cr(Al)N/SiO$_x$ composite layer and transition layers of Cr(Al) and CrN grown between the substrate and the composite layer. These layers were successively sputter-deposited on the Si substrate with different gas flows in the DPCS system. The sputter-deposition was performed at a rotational speed of the substrate as low as 1 rpm, which was not the best for preparing the hard coating, to get the fundamentals

Received: February 4, 2013
Accepted: April 12, 2013
Published: April 12, 2013

 © 2013 American Chemical Society

of deposition process in the DPCS system and to demonstrate its usefulness for fabricating composite films and disclosing the point at issue.

2. EXPERIMENTAL SECTION

The DPCS system has two chambers **A** and **B**, divided by a center wall, for radio frequency (RF) magnetron sputter deposition of different materials and a rotating substrate holder which is placed on top of the dual chambers, as shown in Figure 1.[11] Different gas atmospheres can be provided into chambers **A** and **B** independently. Nine substrates of ~22 mm × ~24 mm are placed on the rotating holder at 154 mm ± ~12 mm from its center. In the present experiment, $Cr_{50}Al_{50}$ and SiO_2 targets were set in the left chamber **A** and the right chamber **B**, respectively, and the holder was rotated at a rotational speed as low as 1 rpm and heated at 250 °C. First, three depositions I, II, and III were successively performed on (001) Si wafer substrates from the CrAl target for 8.2, 29.4, and 36.2 min with flows of Ar (10 sccm), Ar (10 sccm) + N_2 (10 sccm), and Ar (10 sccm) + N_2 (20 sccm) using chamber **A**, as tabulated in Table 1. They are transition layers to promote the adhesion between the substrate and the composite film by changing the composition from metal to nitride, because the composite film aims for hard coating of metal surfaces. During these three depositions, the SiO_2 target was not sputtered with closing a shutter over the target, but Ar gas flow was fed (at 10 or 20 sccm) into chamber **B** in order to suppress gas leak from **A** to **B** through a clearance between the center wall and the substrate holder. Then by operating the SiO_2 chamber **B** and opening its shutter to the holder, the next main deposition IV was carried out for 660 min from the CrAl and SiO_2 targets with flows of Ar (10 sccm) + N_2 (20 sccm) and Ar (20 sccm) at RF powers of 200 and 75 W, respectively, so as to obtain a nominal composition of CrAlN/38 vol% SiO_x. The system worked stably during an operating time as long as ~12 h.

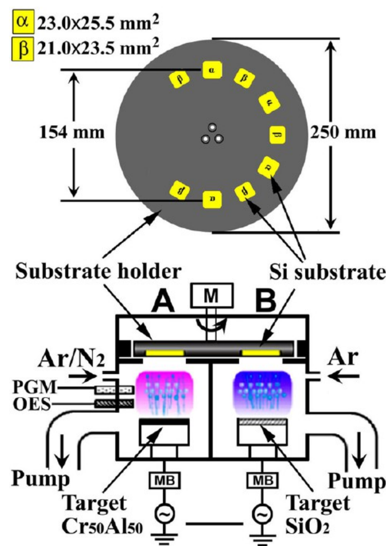

Figure 1. (a) Schematic diagram of a differential pumping cosputtering (DPCS) system with two chambers **A** and **B**. PGM is a process gas monitor, and OES is an optical emission spectroscope. M is a motor for rotating the substrate holder, where Si substrates (α and β) are set. MB is a mechanical pump and a turbomolecular pump to evacuate each chamber to a vacuum better than 8.0 × 10^{-4} Pa prior to deposition.

The sample was thinned using a JEOL IonSlicer EM-09100IS for transmission electron microscopy (TEM) and scanning transmission electron microscopy (STEM). Initial TEM and STEM analysis was performed in a JEM-2800 microscope, attached with a JEOL Centurio (100 mm² Silicon Drift detector) for energy dispersive X-ray spectroscopy (EDS), a Gatan GIF Tridiem for electron energy loss spectroscopy (EELS), and an Orius 200D (model 833) for electron diffraction (ED), followed by atomic scale high-resolution (HR) investigation in a JEOL ARM200F microscope equipped with a cold field emission gun as well as a Centurio and a GIF Quantum for dual spectroscopy.

3. RESULTS AND DISCUSSION

Figure 2a shows a conventional TEM image of the sample prepared on the (001) Si substrate. ED pattern from area **A**, shown in Figure 2b, indicates that the area **A** is the Si substrate with the [110] axis along the incident electron beam, although

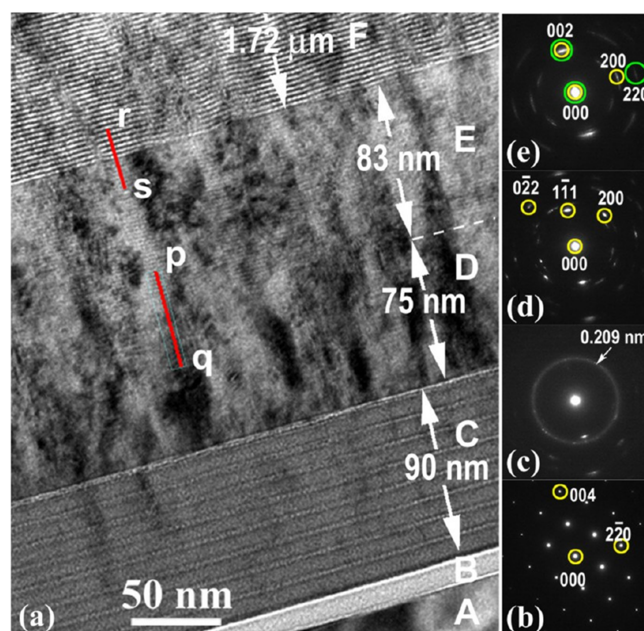

Figure 2. (a) Conventional HR-TEM image of the sample. (b−e) Electron diffraction patterns from areas in layers **A**, **C**, **D**, **E**, and **F**, respectively. In part e, crystals with different orientations exhibit the 200 and 220 reflections, separately. The intensities along lines **p**−**q** and **r**−**s** were measured and shown in Figure 6a and b, respectively.

Table 1. Sputtering-Deposition Conditions for the Transition Layers I, II, and III and Main Composite Layer IV and Structure of the Deposited Films

	chamber **A**: CrAl target				chamber **B**: SiO_2 target				
	Ar	N_2 (sccm)	shutter	power (W)	Ar (sccm)	shutter	power (W)	number of revolution	deposited film
I	10	0	open	200	10	close	0	1	*a*-Al_2O_3 (**B**)
								8	Cr(Al) + *a*-Al_2O_3 (**C**)
II	10	10	open	200	20	close	0	30	CrN + *a*-Al_2O_3 (**D**)
III	10	20	open	200	20	close	0	36	CrN + *a*-Al_2O_3 (**E**)
IV	10	20	open	200	20	open	75	660	Cr(Al)N/*a*-SiO_x (**F**)

several forbidden reflection spots such 002 appear as a result of "Umweganregung". Figure 3a shows a STEM high-angle

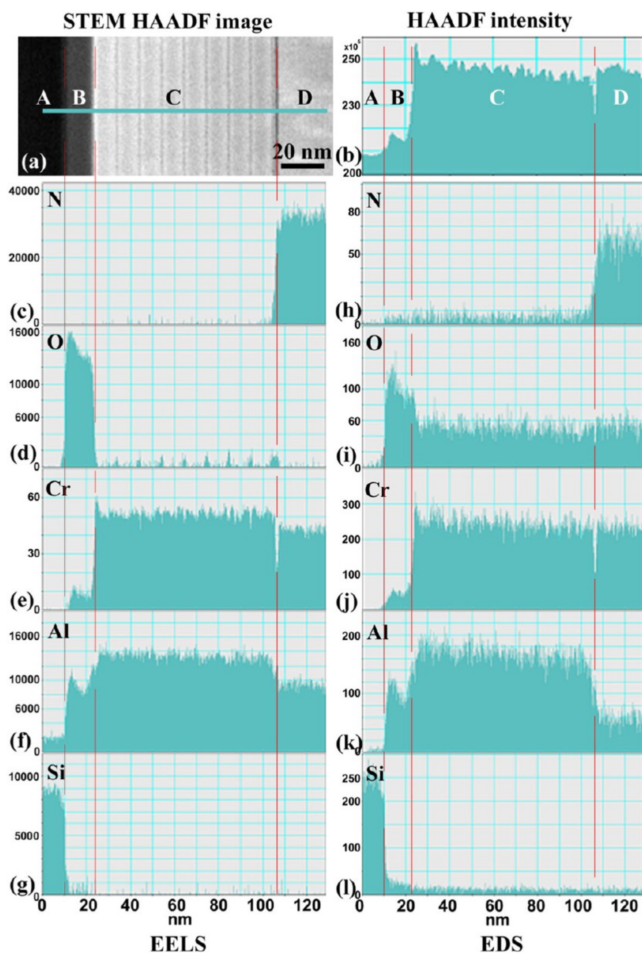

Figure 3. (a) STEM-HAADF image of an area including layers **A**–**D**. (b) Intensity of the HAADF image along the line indicated in part a. (c–g) ELLS intensity profiles of N–K, O–K, Cr–L, Al–K, and Si–K signals along the line indicated in part a, respectively. (h–l) EDS intensity profiles of N–K, O–K, Cr–L, Al–K, and Si–K signals along the line indicated in part a, respectively. The boundaries between the layers are indicated.

annular dark-field (HAADF) image. The HAADF intensity profile and EELS and EDS intensity profiles for N–K, O–K, Cr–L, Al–K, and Si–K signals along the line in Figure 3a are displayed in parts b, c–g, and h–l, respectively. The EELS and EDS were performed along the same line simultaneously. The HAADF images are mainly formed by thermal diffuse scattering of electrons or incoherent imaging of elastically scattered electrons and provide the atomic number (Z) contrast, approximately proportional to the square of the atomic number.[17,18] From the results of the EELS and EDS analyses and HR-TEM in Figures 3 and 4a, layer **B**, which formed in the first revolution of deposition I, is regarded as amorphous (a) aluminum oxide containing a small amount of Cr (and also Si diffused from the substrate). It grew on the Si substrate at an initial sputtering from the CrAl target with Ar (10 sccm) flow. The O_2 gas that possibly leaked in at opening the valve of the Ar cylinder is responsible for the formation of such oxide by working as oxygen ions in the plasma. Most of deposited Cr atoms diffused out toward its surface, which made a sharp peak

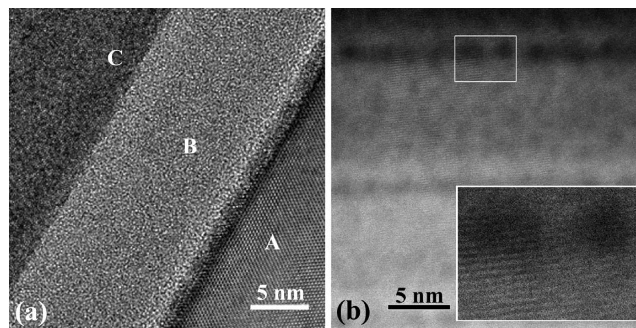

Figure 4. (a) Energy filtered (10 eV) multibeam TEM image of an area including layers **A**, **B**, and **C**. (b) HR STEM-HAADF image of an area in layer **C**. Inset is an enlarged image of the small area indicated by a rectangle.

in the Cr intensity profile (Figure 3e) and strong bright contrast in HAADF image (Figure 3a and b) along the interface between layers **B** and **C**. The O_2 gas may be almost consumed during the first revolution. Layer **C** in Figure 2a also formed by sputtering from the CrAl target with the Ar flow for 8 min (deposition I). The layer is composed of 8 sublayers that correspond to the 8 revolutions. The total thickness is 90 nm for the nominated thickness of 0.1 μm. Therefore, the growth rate of the layer was ∼11 nm/rev or ∼11 nm/min, which is quite a bit larger than that of the other layers mentioned below, because the layer C was deposited by nonreactive sputtering. EELS and EDS in Figure 3 indicate that layer **C** is composed of Cr, Al, and a small amount of O. The ED pattern from layer **C** is shown in Figure 2c, which exhibits spotty rings and halos although some diffraction spots from the neighboring layer **D** appear as a result of the spherical aberration of the objective lens. The spotty rings can be ascribed to Cr fine particles, and the halos may be ascribed to amorphous oxide. The Cr particles are of *bcc* Cr. The lattice parameter evaluated from the observed diffraction rings; however, a = 0.294 nm, which is about 2% larger than 0.28839 nm in the International Center Diffraction Data (ICCD) pattern: 00-006-0694, due to substitution of Al atoms on Cr sites and other impurity atoms. The amorphous oxide is mainly aluminum oxide since the spacings of (113) α-Al_2O_3 and (400) γ-Al_2O_3 correspond to the halo. An HR STEM-HAADF image shown in Figure 4b indicates lattice fringes in the Cr(Al) particles. It also reveals that the a-aluminum oxide particles with sizes of 1.5 nm or less, which show dark contrast, formed within sublayers and along the boundaries between the sublayers. It may be noted that the HR STEM-HAADF image can identify these thin oxide layers although conventional TEM and HR-TEM images exhibit wider contrast due to effects of diffraction contour and Fresnel diffraction. By geometry of the DPCS system (Figure 1), the substrate rotating at 1 rpm was exposed by plasma only less than 20 s during 1 revolution, and it was in ambient atmospheres without plasma in the CrAl chamber **A** for ∼10 s and in the SiO_2 chamber **B** for the rest ∼30 s. During ∼40 s the a-aluminum oxide particles could form by surface oxidation of just deposited film. The O–K signals in Figure 3d depict the a-aluminum oxide particle layers on the boundaries, which correspond to the narrow dark lines in HAADF image in Figure 3a. Brighter contrast around these boundaries in Figures 3a and 4b may be ascribed to Cr atoms which were left behind for the formation of aluminum oxide on the boundaries.

dx.doi.org/10.1021/am400477f | ACS Appl. Mater. Interfaces 2013, 5, 3833–3838

D in Figure 2a is the layer that started by an additional injection of N_2 gas flow of 10 sccm (deposition II), and **E** is a layer grown at deposition III where the N_2 flow rate was increased to 20 sccm. The ED pattern in Figure 2d indicates that layers **D** and **E** are composed of CrN crystals. Their lattice parameter was estimated to be a = 0.4149 nm, which is the same as that (a = 0.414900 nm) of the NaCl-type CrN reported in ICCD pattern: 03-065-2899. From the diffraction contrasts in layers **D** and **E** in Figure 2a, they seem to grow in columns with a fiber structure along the $[1\bar{1}1]$ zone axis. In Figure 5a and b and their insets, fringes are clearly observed in layer **E**. The number of the fringes in layer **E** corresponds to the number of revolutions of the substrate, 36. Similarly 29 fringes appear with weak contrast in layer **D**. From the observed spacings of the fringes, the growth rate was estimated to be ~2.4 nm/rev for layer **E** and ~2.6 nm/rev for layer **D**. As is well-known, the formation and growth of the nitride by reactive sputtering are very slow as compared with the deposition of metal Cr by nonreactive sputtering in layer **C**. EELS and EDS in Figure 6 (also Figure 3) reveal that layers **D** and **E** include N atoms, confirming the formation of the CrN. Figure 7a shows a STEM-HAADF image of layers **D** and **E**. Since the deposited nitride was almost pure CrN, the excess Al atoms formed *a*-aluminum oxide with the dark contrast on the boundaries between CrN sublayers in Figure 5, similar to the thin *a*-aluminum oxide layers in layer **C**. The dark contrast along the interface between **C** and **D** in Figure 3a also indicates that an *a*-aluminum oxide layer formed in a time of about 1 min for which the shutter in chamber **A** was closed for arrangement of the deposition II. Although neither Cr nor Al was deposited for this time, the *a*-aluminum oxide layer formed on the surface of **C** by residual oxygen atoms in the atmosphere. The composite films usually aim at surface coatings of metals such as steel.[10] These transition layers, where the composition gradually changes from metal (Cr) to nitride (CrN), are appropriate for the nitride film coating of the metal surface.

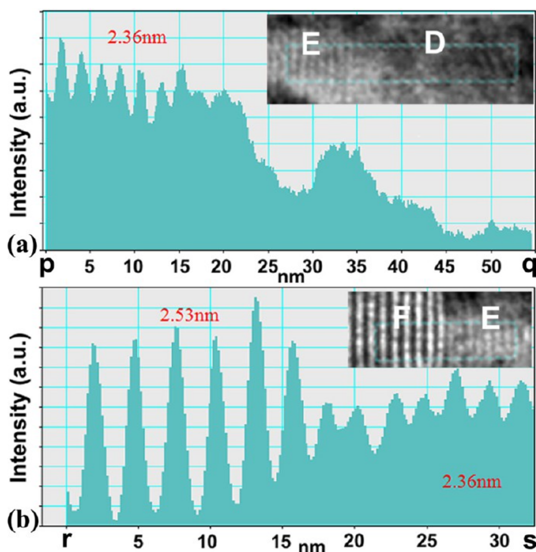

Figure 5. (a) Intensity line profile along **p**−**q** indicated in areas **E** and **D** in Figure 2. (inset) Enlarged image of an area including line **p**−**q**. (b) Intensity line profile along **r**−**s** indicated in areas **F** and **E** in Figure 2. (inset) Enlarged image of an area including line **r**−**s**.

Layer **F** formed by 660 revolutions of the CrAl deposition and the SiO_2 deposition (deposition IV), which are seen in the HR-TEM image in Figure 2a and its intensity line profile along **rs** in Figure 5b. The layer grew at an average rate of ~2.6 nm/

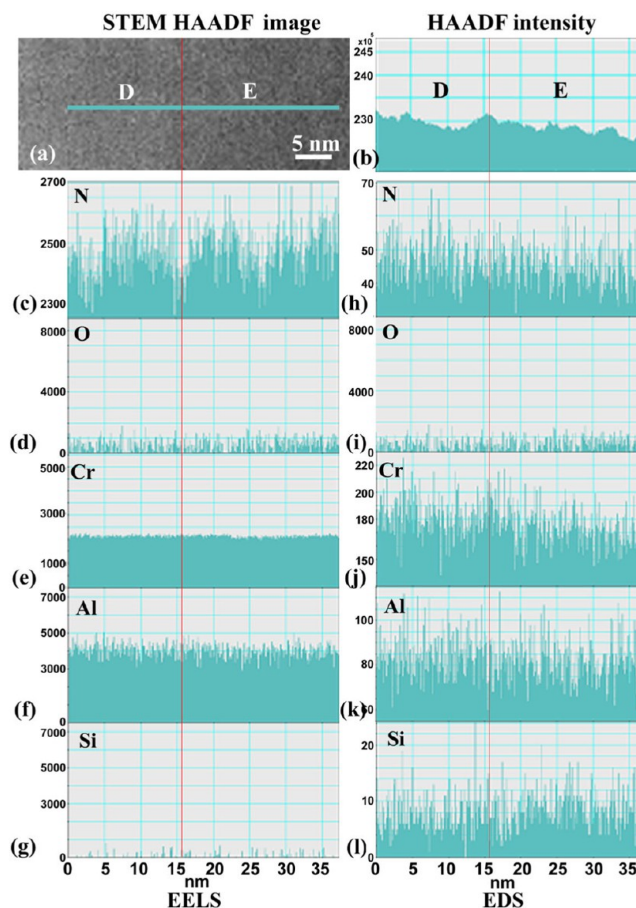

Figure 6. (a) STEM-HAADF image of an area including layers **D** and **E**. (b) Intensity of the HAADF image along the line indicated in part a. (c−g) ELLS intensity profiles of N−K, O−K, Cr−L, Al−K, and Si−K signals along the line indicated in part a, respectively. (h−l) EDS intensity profiles of N−K, O−K, Cr−L, Al−K, and Si−K signals along the line indicated in part a, respectively. The boundary between **D** and **E** layers is indicated.

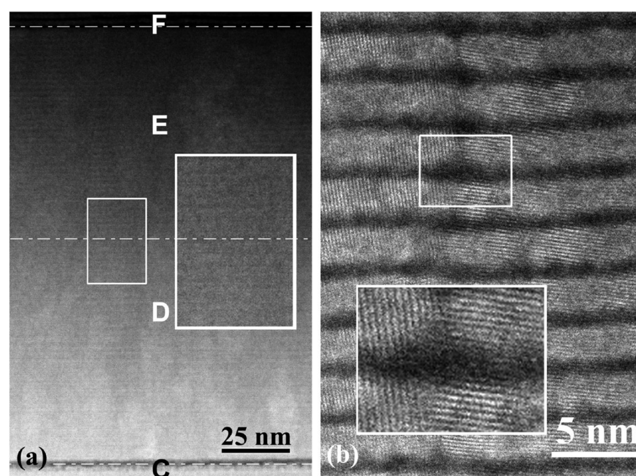

Figure 7. (a) STEM HAADF image of layers D and E. (inset) Enlarged image of the small area indicated by a rectangle. (b) HR STEM-HAADF image of an area in layer **F**. (inset) Enlarged image of the small area indicated by a rectangle.

rev, although the spacing near layer **E** is 2.53 nm as shown in Figure 5b. Line profiles of EELS and EDS shown in Figure 8 indicate that bright bands in STEM-HAADF image are rich with Cr, Al, and N, and dark bands are rich with Si and O. The ED pattern in Figure 2e reveals that layer **F** also included NaCl-type CrN crystals. However, the lattice parameter is a little different from 0.4149 nm of CrN in layer **D** and **E** but 0.402 nm as small as 3%. It must be Cr(Al)N, containing substituted Al atoms on Cr sites.[19] From the HR-HAADF image in Figure 7b, layer F seems to take a multilayer structure of Cr(Al)N layers with bright contrast and *a*-silicon oxide layers with dark contrast, whose thicknesses were ~1.6 and ~1 nm, respectively. This is, however, Cr(Al)N/SiO_x nanocomposite, as discussed below. Owing to the deposition of *a*-SiO_x, the Al atoms sputter-deposited from the CrAl target are hardly diffused out from the sublayer and rather remain to make the Cr(Al) phase.

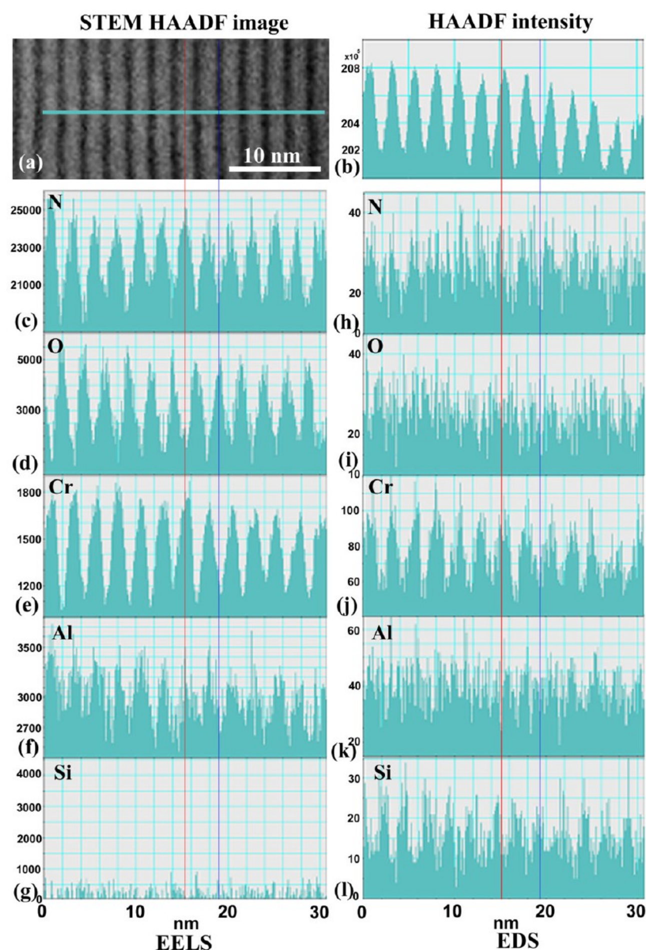

Figure 8. (a) STEM-HAADF image of an area in layer **F**. (b) Intensity of the HAADF image along the line indicated in part a. (c−g) ELLS intensity profiles of N−K, O−K, Cr−L, Al−K, and Si−K signals along the line indicated in part a, respectively. (h−l) EDS intensity profiles of N−K, O−K, Cr−L, Al−K, and Si−K signals along the line indicated in part a, respectively.

Through the two underlayers (**D** and **E**) and the composite layer **F**, CrN and Cr(Al)N crystals grew with columnar structure (see Figure 2a). The *a*-oxide films in these layers were thin (<~1 nm) and grew as separated particles rather than continuous layers so that the nitride crystals could grow continuously into the following sublayer even through the spaces between the amorphous particles, keeping a coherent lattice relation, as seen in Figures 4b and 7b. In other words, the small nitride crystals in layers **D**, **E**, and **F** included *a*-aluminum oxide particles. That is the reason why layer F is regarded as Cr(Al)N/SiO_x nanocomposite.

According to our mechanical measurements, which was made using a microtriangular Berkovitch diamond pyramid in a nanoindentation system (FISCHERSCOPE H100C XYp) at room temperature, the indentation hardness of the present sample of Cr(Al)N/38 vol % SiO_x prepared at 1 rpm was ~25 GPa, while that of Cr(Al)N/38 vol % SiO_x prepared at 12 rpm was ~33 GPa.[20] Faster rotation would make each sublayer of the composite films thinner, resulting in the formation of fine Cr(Al)N crystallites enclosed with amorphous silicon oxides, which makes the composite films harder. Indeed the hardness of a Cr(Al)N/17 vol % SiO_x nanocomposited film prepared at 12 rpm reached 46 GPa, which is comparable to the hardness of the superlattice CrN/AlN coating reported by Lin et al.[15] Details of the structure and mechanical property of these practical coating films will be reported elsewhere.

The EELS and EDS provided complementary results: EELS gave high space-resolved data while EDS performed using the detector as wide as 100 mm^2 gave high sensitive ones.

4. CONCLUSION

We have identified the structure of various films prepared continuously in the DPCS system where the substrate was rotated at 1 rpm, by analytical electron microscopy. The following are conclusions, which are briefly indicated in Table 1.

(1) The layer that was sputter-deposited on the (001) Si substrate at 250 °C from the CrAl target with the Ar flow for 8 min was composed of Cr(Al) fine particles and amorphous aluminum oxides. The layer comprised eight sublayers ~11 nm thick, corresponding to the eight revolutions. Amorphous aluminum oxide particle layers 1.5 nm thick or less formed within the sublayers and along the interfaces between them. Since the working time of the sputtering deposition was 20 s or less during one revolution, the aluminum oxide interface layers formed, during the rest time ~40 s, by adsorption of residual O_2 gas.

(2) The deposited layer that started by an injection of N_2 gas flow was composed of CrN crystals with a column structure along the $[1\bar{1}1]$ axis. As the N_2 flow rate was increased from 10 to 20 sccm, the growth rate decreased from ~2.6 to ~2.3 nm/revolution. These layers also comprised thin film layers of amorphous aluminum oxide between the sublayers, which formed by a way similar to the forming process of the amorphous interface layers mentioned in 1.

(3) The layer that was sputter-deposited from the CrAl and SiO_2 targets with Ar + N_2 flows and an Ar flow, respectively, was Cr(Al)N/SiO_x nanocomposite films. The thicknesses of the Cr(Al)N and SiO_x films were ~1.6 and ~1 nm, respectively.

The structure analysis of the films prepared at a rotational speed as low as 1 rpm has revealed the formation process of ultrathin films in the DPCS system and disclosed some points at issue such as the formation of unexpected oxide interfaces. This promises that harder coating films can be fabricated by

controlling rotational speed and discharge of gases as well as target materials.

AUTHOR INFORMATION

Corresponding Author

*E-mail: kawasaki@jeol.com.

Present Address

○M.S.: 1-297 Wakiyama, Enmyoji, Kyoto 618−0091, Japan.

Notes

The authors declare no competing financial interest.

REFERENCES

(1) Oelhafen, P.; Schüler, A. *Sol. Energy* **2005**, *79*, 110−121.
(2) Martinu, L.; Poitras, D. *J. Vac. Sci. Technol. A* **2000**, *18*, 2619.
(3) Battaglin, G.; Cattaruzza, E.; Gonella, F.; Polloni, R.; Scremin, B. F.; Mattei, G.; Mazzoldi, P.; Sada, C. *Appl. Surf. Sci.* **2004**, *226*, 52−56.
(4) Wang, C. M.; Hsieh, J. H.; Fu, Y.; Li, Q. C.; Chen, T. P.; Lam, U. T. *Ceram. Int.* **2004**, *30*, 1879−1883.
(5) Fujimori, H.; Mitani, S.; Ohnuma, S. *J. Magn. Magn. Mater.* **1996**, *156*, 311−314.
(6) Watanabe, K.; Nakanishi, N.; Yamazaki, T.; Yang, J. R.; Y. Huang, S.; Inoke, K.; Hsu, J. T.; Tu, R. C.; Shiojiri, M. *Appl. Phys. Lett.* **2003**, *82*, 715−717.
(7) Chen, M. J.; Shih, Y. T.; Wu, M. K.; Chen, H. C.; Tsai, H. L.; Li, W. C.; Yang, J. R.; Kuan, H.; Shiojiri, M. *IEEE Trans. Electron Devices* **2010**, *57*, 2195−2202.
(8) Hsieh, J. H.; Chang, C. C.; Chang, Y. K.; Cherng, J. S. *Thin Solid Films* **2010**, *518*, 7263−7266.
(9) Holubář, P.; Jílek, M.; Šíma, M. *Surf. Coat. Technol.* **1999**, *120/121*, 184−188.
(10) Nose, M.; Kawabata, T.; Khamseh, S.; Matsuda, K.; Fujii, K.; Ikeno, S.; Chiou, W. A. *Mater. Trans.* **2010**, *51*, 282−287.
(11) Nose, M.; Kurimoto, T.; Saiki, A.; Matsuda, K.; Terayama, K. *J. Vac. Sci. Technol. A* **2012**, *30*, 011502.
(12) Musil, J. *Surf. Coat. Technol.* **2000**, *125*, 322−330.
(13) Mayrhofer, P. H.; Mitterer, C.; Hultman, L.; Clements, H. *Prog. Mater. Sci.* **2006**, *51*, 1032−1114.
(14) Veprek, S.; Veprek-Heijman, M. G. J. In *Nanostructured Coatings*; Cabaleiro, A. A., De Hosson, J. T. M., Eds.; Springer: New York, 2006; Chapter 9, pp 347−406.
(15) Lin, J.; Moore, J. J.; Moerbe, W. C.; Pinkas, M.; Mishra, B.; Doll, G. L.; Sproul, W. D. *Int. J. Refract. Met. Hard Mater.* **2010**, *28*, 2−14.
(16) Stüber, M.; Albers, U.; Leiste, H.; Seemann, K.; Ziebert, C.; Ulrich, S. *Surf. Coat. Technol.* **2008**, *203*, 661−665.
(17) Pennycook, S. J.; Nellist, P. D. In *Impact of Electron and Scanning Probe Microscopy on Materials Research*, Rickerby, D. G., Valdrè, G., Valdrè, U., Eds.; Kluwer Academic Publishers: Dordrecht, 1999; pp 161−207.
(18) Shiojiri, M.; Saijo, H. *J. Microsc.* **2006**, *223*, 172−178.
(19) Kimura, A.; Kawate, M.; Hasegawa, H.; Suzuki, T. *Surf. Coat. Technol.* **2003**, *169/170*, 367−370.
(20) Nose, M.; Chiou, W. A.; Takabatake, H.; Satho, T.; Kawabata, T.; Matsuda, K. *Microsc. Microanalysis.* **2012**, *18* (Suppl. 2), 1696−1697.